PERGAMON

International Journal of Heat and Mass Transfer 42 (1999) 2557–2569

International Journal of HEAT and MASS TRANSFER

Heat and mass transfer with phase change in a porous structure partially heated: continuum model and pore network simulations

C. Figus, Y. Le Bray, S. Bories, M. Prat

Institut de Mécanique des Fluides de Toulouse, UMR CNRS-INP/UPS no. 5502, Avenue du Professeur Camille Soula, 31400 Toulouse, France

Received 16 October 1997; in final form 8 October 1998

Abstract

The heat and mass transfer within a porous structure with partial heating and vaporization on the upper surface is studied numerically. Two models are presented: a continuum (Darcy) model and a pore network model. Both approaches show that the liquid-vapor front enters inside the porous structure. When the structure is characterized by a single pore size, the continuum model and the pore network model lead to the same stationary solution and the liquid–vapor front is smooth. When there exists a pore size distribution, pore network simulations show that the front resembles fractal fronts typical of invasion percolation. Implications of the results to capillary pumped loops (CPL) are discussed. In particular, the results indicate that capillary fingering may limit the operating range of CPL.

Nomenclature

d length [m]
d^* thermal network mesh size [m]
g flow conductance [m^2]
k permeability [m^2]
L latent heat of vaporization [J kg^{-1}]
L_f length of the fin [m]
L_x length of the porous structure in the x-direction [m]
L_y length of the porous structure in the y-direction [m]
p pressure [Pa]
p_c capillary pressure [Pa]
R index of the pore structure disorder
s bond cross section [m^2]
S cross section (thermal network) [m^2]
T temperature [K]
T_{sat} saturation temperature [K]
T_0 temperature at the entrance of the wick [K]
ΔT $T-T_0$ [K]
u bond average velocity [m s^{-1}]
v filtration velocity [m s^{-1}].

Greek symbols

λ thermal conductivity [W m^{-1} K^{-1}]
Γ vapor–liquid front
ε porosity
μ viscosity [Pa s^{-1}]
ρ density [kg m^{-3}]
σ surface tension [N m^{-1}]
ϕ heat load [W m^{-2}]
ϕ_m mass source term [kg m^{-2} s^{-1}]
Ω_f liquid domain
Ω_v vapor domain.

Subscripts/superscripts

ef effective
l liquid
ref reference
v vapor
s solid
sat saturation.

1. Introduction

The study presented in this paper is related to the evaporator of capillary pump loops (CPL). Capillary

* Corresponding authors. Tel.: 00 33 61 28 58 77; fax: 00 33 61 28 58 78.

E-mail addresses: bories@imft.fr (S. Bories), prat@inft.fr (M. Prat)

0017–9310/99/$ - see front matter
PII: S0017–9310(98)00342–1

pump loops have been developed as an attractive system for the thermal management of spacecraft with high power loads [1]. Typically, a CPL consists of an evaporator and a condenser interconnected by a system of pipe (Fig. 1). Figure 2 shows the cross section of a classic cylindrical evaporator. Under the influence of the heat load applied on the external surface of the metallic grooved structure, the liquid contained in the porous wick vaporizes, the vapor flows through the grooves towards the condenser and the condensed liquid returns to the evaporator owing to the capillary pressure across the meniscii that form at the surface or inside the porous wick. By choosing a working fluid having a large heat of vaporization, ammonia for example, one may expect to dissipate significant heat flux. In such a system, the evaporator is the most important part. Therefore, the optimal design of CPL requires a thorough understanding of the physical phenomena occurring within the evaporator. This is the primary objective of the present paper. Additionally, the influence of various factors, such as the transport properties and/or the structural characteristics of the wick are partially explored. Our study is not the first dedicated to this problem. For basically the same two-dimensional system as the one considered in our study, Cao and Faghri [2] developed an analytical solution. This solution is however restricted to homogeneous wicks and situations in which the wick is completely saturated by liquid. The fact of considering a two-dimensional model is supported by the numerical results presented in [3] (note, however, that the results presented in [3] were obtained within the framework of a continuum model and not pure network models). In that later study, Cao and Faghri presented a conjugate analysis of a system including a segment of wick and a groove. In particular, influence of the working fluid on the vapor flow in the groove was studied. Again, this study was restricted to situations where the change of phase takes place at the groove–wick interface and not within the wick. The same year, Demidov and Yatsenko [4] presented a numerical study showing that vapor zones can take place within the wick under the fins. The study of Demidov and Yatsenko was carried out at the continuum or Darcy level. For the present study, we developed a continuum level model which is similar to the one presented in [4]. Our method of solution is, however, different. In addition, we developed a pore network model. To the best of our knowledge, a pore network model has never been used before in the context of capillary evaporators. The main motivation for developing a pore network model stems from recent studies on liquid–vapor phase change in capillary porous media, [5–7]. These studies show that fractal patterns of the invasion percolation type [8], could be expected when capillarity dominates the process (in the system under study, the capillary forces are clearly the dominant forces). It is well known that the continuum approach to porous media is not adapted for modeling a system close to a percolation threshold. In such a case, pore network models are much more appropriate. In particular, the pore network simulations show that capillary fingering may lead to deprime of the evaporator even if the working conditions are far from the nominal capillary capacity of the wick. Also, it may be observed

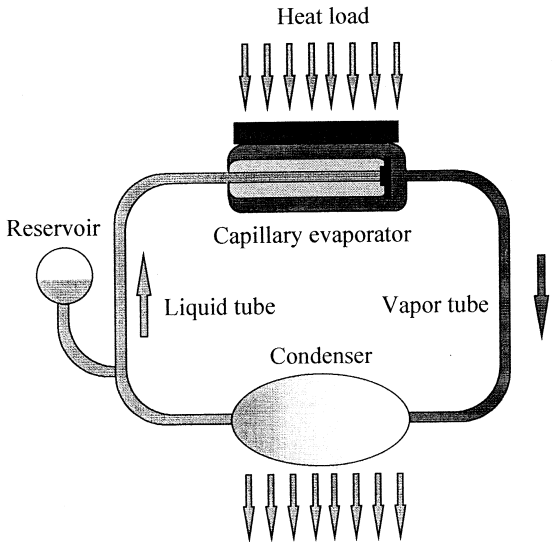

Fig. 1. Schematic of a CPL.

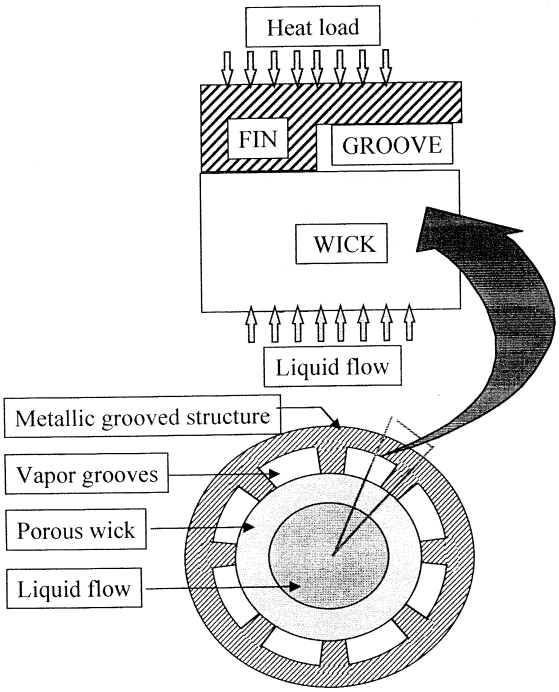

Fig. 2. Cylindrical evaporator.

that typical evaporator geometries have groove and fin dimensions of about 1 mm. With typical pore diameters of the order of 10 μm and particle diameters ranging to 100 μm, there may be only 10–20 pores per mm [9]. Therefore, pore networks containing roughly the same number of pores as in a representative section of a real system can be considered easily. The pore network approach is also helpful for determining the conditions under which the continuum model presented in Section 3 is valid. It is shown that this continuum model is in fact appropriate only when the pore size distribution is extremely narrow.

2. Problem statement

Due to symmetry, the study is restricted to a segment of the wick as sketched in Fig. 2. On the basis of the study of Cao and Faghri [3], a two-dimensional geometry is considered. Only stationary solutions are studied. Due to the high thermal conductivity of the metallic fin compared to the thermal conductivity of the vapor within the groove, the temperature within the wick reaches the saturation temperature first under the fin. In agreement with Demidov and Yatsenko [4], this leads to the formation of a vapor zone. Hence, a typical computational domain is shown in Fig. 3. In Fig. 3, the vapor–liquid front is shown as a smooth line separating a liquid zone from a vapor zone. We shall see that such a representation is not always correct, owing to capillary effects. This is, however, a useful representation within the framework of the continuum model presented hereafter.

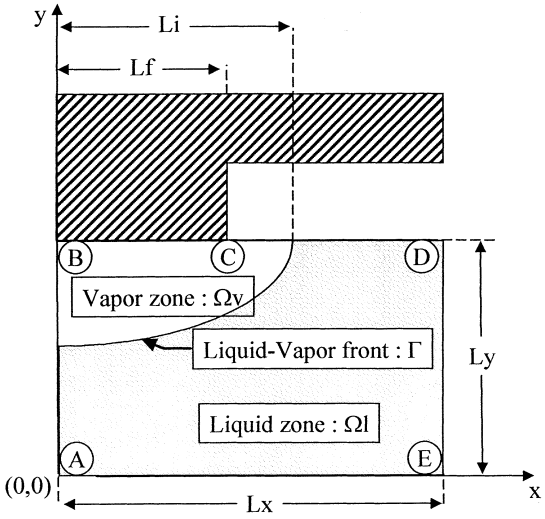

Fig. 3. Computational domain.

3. Continuum level model

3.1. Differential equations

The continuum level model is based on the following main assumptions: negligible gravity effect, local thermal equilibrium between the solid phase and the vapor or the liquid, radiative and convective heat transfers negligible compared to conductive heat transfer and latent heat transfer. The liquid vapor transition takes place at a front of zero thickness. This last assumption is associated with porous structures characterized by a single pore size. Incompressible flows are assumed in the liquid phase as well as in the gas phase. This last assumption is not strictly correct since pressure and temperature variations occur within the vapor zone. We note that a similar assumption was made by Demidov and Yatsenko [4]. Under these assumptions, the governing equations, where l corresponds to liquid and v to vapor, read

Continuity and momentum (Darcy) equations,

$$\nabla \cdot v_i = 0 \text{ in } \Omega_i \text{ with } i = \mathrm{l}, \mathrm{v} \tag{1}$$

$$\mathrm{v}_i = -\frac{k}{\mu_i}\nabla p_i \text{ in } \Omega_i \text{ with } i = \mathrm{l}, \mathrm{v} \tag{2}$$

which can be combined to obtain

$$\nabla^2 p_i = 0 \text{ in } \Omega_i \text{ with } i = \mathrm{l}, \mathrm{v} \tag{3}$$

Energy equation,

$$\nabla^2 T_i = 0 \text{ in } \Omega_i \text{ with } i = \mathrm{l}, \mathrm{v} \tag{4}$$

Conditions on the front.

$$T_l = T_\mathrm{v} = T_\mathrm{sat} \text{ at } \Gamma \tag{5}$$

where T_sat is the saturation temperature.

$$p_\mathrm{v} - p_l = p_\mathrm{c} \text{ at } \Gamma \tag{6}$$

where p_c is the capillary pressure

$$\rho_l v_l \cdot n = \rho_\mathrm{v} v_\mathrm{v} \cdot n \text{ at } \Gamma \tag{7}$$

$$\lambda_\mathrm{v}^\mathrm{ef} \nabla T_\mathrm{v} \cdot n - \lambda_l^\mathrm{ef} \nabla T_l \cdot n = \rho_l v_l \cdot nL \text{ at } \Gamma \tag{8}$$

where n is the normal unit vector at the front. $\lambda_\mathrm{v}^\mathrm{ef}$ and λ_l^ef are the effective thermal conductivity of the porous medium saturated by liquid and by vapor respectively. These thermal conductivities were estimated according to a parallel arrangement model, i.e. $\lambda_i^\mathrm{ef} = (1-\varepsilon)\lambda_\mathrm{s} + \varepsilon\lambda_i$ with $i = \mathrm{l},\mathrm{v}$ and where ε is the wick porosity, λ_s is the solid thermal conductivity and λ_i corresponds to the fluid thermal conductivity. In Equation (8), L is the latent heat of phase change.

Local thermodynamic equilibrium equation at the front (Clausius–Clapeyron equation),

$$p_l = p_\mathrm{sat} = p_\mathrm{ref} \exp(-A(1/T_\mathrm{sat} - 1/T_\mathrm{ref})) \text{ at } \Gamma \tag{9}$$

where p_ref and T_ref are reference pressure and temperature.

Boundary conditions

$$\text{At } y = 0, \quad p_l = p_0, \quad T_l = T_0 \tag{10}$$

$$\text{At } x = 0 \text{ and } x = L_x, \quad \frac{\partial p_i}{\partial x} = 0, \quad \frac{\partial T_i}{\partial x} = 0, \quad i = \text{l, v} \tag{11}$$

$$\text{At } y = L_y \text{ and } 0 \leqslant x \leqslant L_f, \quad \frac{\partial p_i}{\partial y} = 0, \quad \lambda_i^{ef} \frac{\partial T_i}{\partial y} = \phi, \quad i = \text{l, v} \tag{12}$$

$$\text{At } y = L_y \text{ and } L_f \leqslant x \leqslant L_i, \quad p_v = p_l, \quad \frac{\partial T_v}{\partial y} = 0 \tag{13}$$

$$\text{At } y = L_y \text{ and } L_i \leqslant x \leqslant L_x, \quad \frac{\partial p_l}{\partial y} = 0, \quad T_l = T_l \tag{14}$$

Some compromise is necessary in terms of boundary conditions if one wants to consider only an element of the wick and not the whole loop. In Equation (13), p_l is the pressure in the groove. We also have $p_0 = p_l - \Delta p$ where Δp denotes the pressure loss within the loop. As can be seen from Equations (12) and (13), the heat flux through the groove is assumed to be negligible compared to the heat flux coming through the fin (note that the thermal conductivity of the fin is about two orders of magnitude greater than the thermal conductivity of the vapor). Equation (14) states that a saturation temperature equal to T_l is imposed at $y = L_y$ and $L_i \leqslant x \leqslant L_x$. We also assumed that the mass flux at $y = L_y$ and $L_i \leqslant x \leqslant L_x$, Equation (14), was negligible compared to the mass flux crossing the section of the liquid–vapor interface located within the wick.

3.2. Numerical procedure

The conservation equations and boundary conditions were solved by applying the Galerkin finite element method [10]. The additional difficulty here is that the front position is unknown. This difficulty was dealt with a front tracking method. The developed front tracking method is based on a moving structured grid that progressively adjusts to the front shape. This implies to regenerate the grid at each step. The overall numerical procedure can be summarized as follows:

(1) Specify an initial arbitrary liquid–vapor front location.
(2) Generate the grid.
(3) Solve the pressure Equation (3).
(4) Compute the velocity and the flow rate, Equation (2).
(5) Solve the energy Equation (4).
(6) Compute the new front location.
(7) Go back to step 2.
(8) Repeat the procedure until convergence.

A 91×91 elements grid turned out to be satisfactory, see [11] where all the details regarding the numerical procedure can be found.

3.3. Results

The results presented in what follows were obtained with ammonia as the working fluid. The porosity of the wick is $\varepsilon = 0.4$. Its permeability is $k = 10^{-13}$ m^2. The thermal properties taken in the computation as $\lambda_s = 0.4$ W m^{-1} K^{-1}, $\lambda_l = 0.5$ W m^{-1} K^{-1}, $\lambda_v = 0.05$ W m^{-1} K^{-1}, $L = 1.13\ 10^6$ J kg^{-1}. The geometric parameters are $L_f = 2 \times 10^{-3}$ m, $L_x = L_y = 5 \times 10^{-3}$ m. The boundary conditions were specified as follows: $T_0 = 26°C$, $T_l = 30°C$, $P_0 = P_{sat}(T_l) - 40$ Pa, $P_l = P_{sat}(T_l)$. ϕ is varied in the range 4500–9000 W m^{-2}.

Figure 4 shows the temperature field and the front location for $\phi = 6000$ W m^{-2}. Figures 5 and 6 display

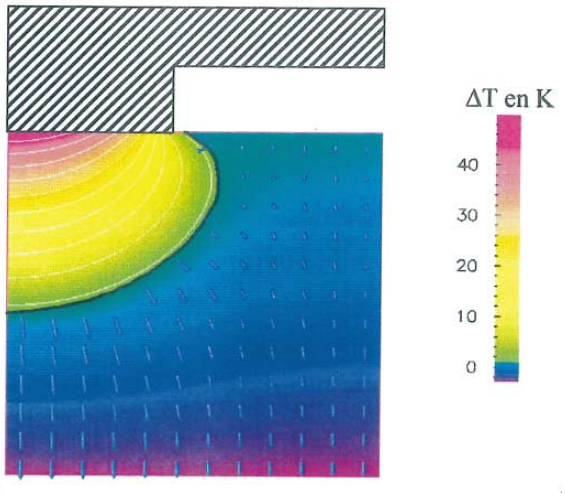

Fig. 4. Temperature field (continuum model) $\Delta T = T - T_0$.

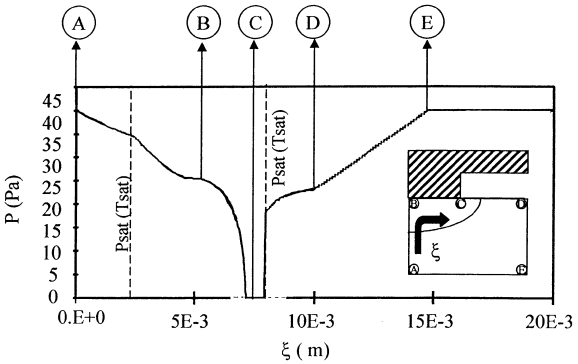

Fig. 5. Pressure distribution along the boundary of the computational domain. ξ is the curvilinear coordinate along the boundary of the computational domain ($\xi = 0$ at point A). (See Fig. 3 for definition of points A, B, C, D, E.)

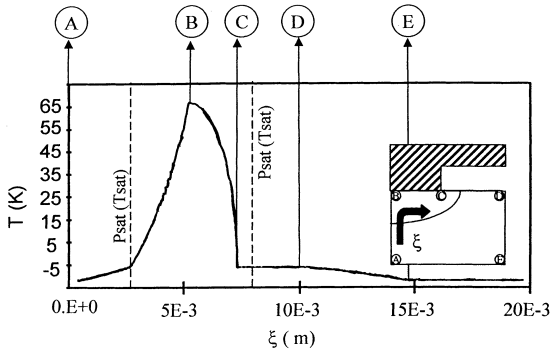

Fig. 6. Temperature distribution along the boundary of the computational domain. ξ is the curvilinear coordinate along the boundary of the computational domain ($\xi = 0$ at point A). (See Fig. 3 for definition of points A, B, C, D, E.)

the pressure and temperature distributions along the boundary of the computational domain. As indicated in Fig. 5, the pressure drop is higher in the vapor zone than in the liquid zone. This is consistent with the fact that the kinematic viscosity of the vapor is here larger than the kinematic viscosity of the liquid ($v_l = 2 \times 10^{-7}$ m^2 s^{-1}, $v_v = 1.1\ 10^{-6}$ m^2 s^{-1}). The much greater pressure drop in the region of corner point C is consistent with the fact that all the vapor produced at the front should escape through the relatively small cross section $L_f \leqslant x \leqslant L_i$. Figure 6 shows that the vapor is superheated except on the front where the temperature is equal to the saturation temperature. Consistently with the development of a vapor zone underneath the fin, the maximum temperature is reached on the wick–fin interface.

Figure 7 presents the evolution of the front location as a function of the heat load. Not surprisingly, the size of the vapor zone increases with ϕ. Naturally, as depicted in Fig. 8, the fin temperature also increases with ϕ. Additional results can be found in [11, 12]. In particular, the influence of a thin gap between the fin and the wick was also explored by means of the continuum model [12]. This gap allows the vapor to escape from the wick and therefore leads to reduce significantly the fin temperature for a given heat load.

4. Pore network simulation

4.1. Model formulation

Pore network simulation has been extensively used for studying immiscible displacements as well as many other transport processes in porous media [13]. As mentioned before, such models have also been used for studying liquid–vapor phase change phenomena [5, 6, 14]. In these works, however, the change of phase was driven by mass

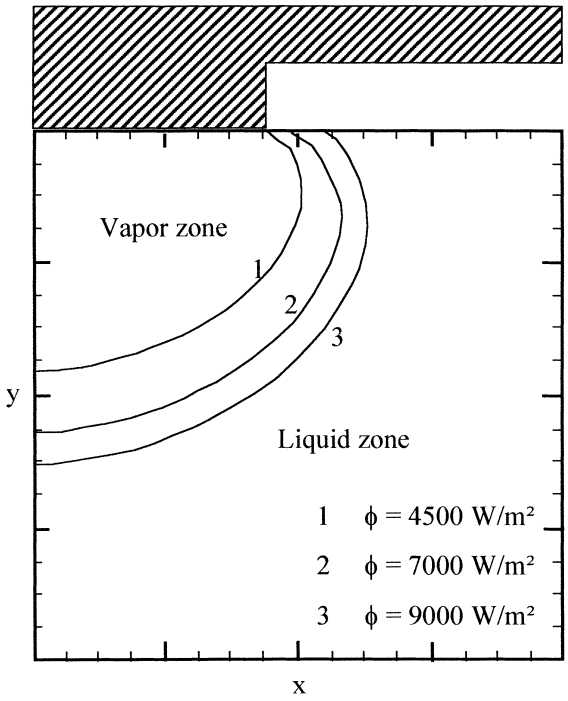

Fig. 7. Evolution of the front position as a function of heat load.

transfer under isothermal or quasi-isothermal conditions. To the best of our knowledge, the first pore network models taking into account the heat transfer in the context of liquid–vapor phase change in porous media are the model used in the present study [11, 15] and the one developed by Satik and Yortsos [16]. In this type of model, the pore space is modeled by a network of sites (pores) and bonds (throats). A square lattice was used for the present study, Fig. 9.Taking into account the conductive heat transfer in the solid requires to consider a complementary square network as explained below. As for the continuum model, gravity effects are neglected. The key elements of the pore-network model are as follows:

Mass and momentum balances

Using technique similar to a standard finite volume technique, the continuity equation can be discretized as follows at node i:

$$\sum_k \rho_{ki}^j u_{ki}^j s_{ki} = 0 \quad k = 1,4 \tag{15}$$

where $j = $ l (liquid) or v (vapor) depending on the fluid occupying node i. k varies from 1 to 4 where 1 (respectively 2, 3 and 4) corresponds to the bond located to the north (respectively east, south, west) of node i. s_{ki} is the cross section of bond ki. u_{ki}^j is the average velocity in bond ki, which is expressed by a Poiseuille-type law,

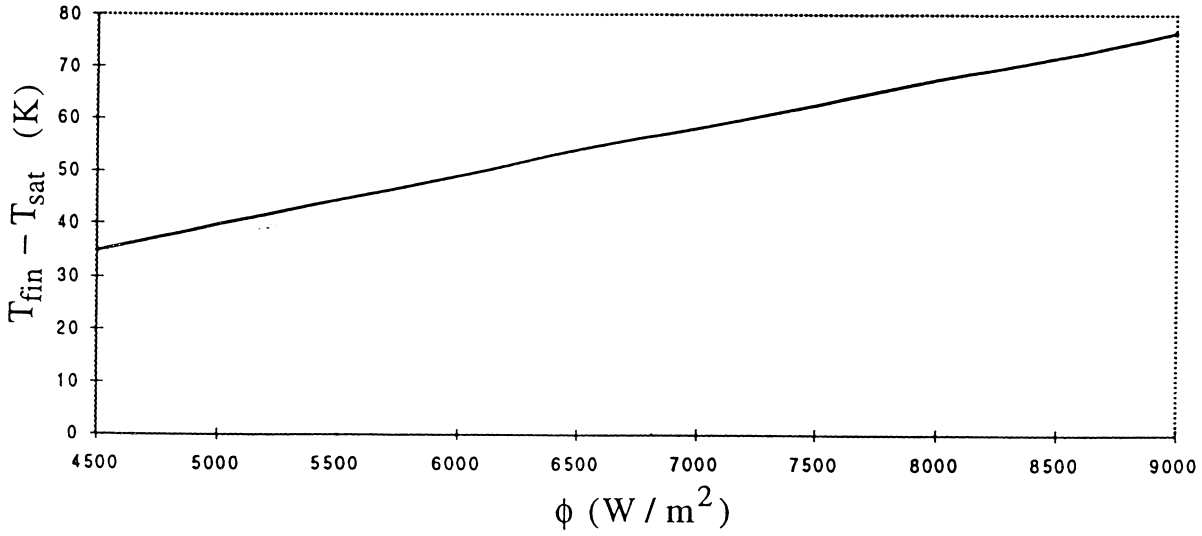

Fig. 8. Evolution of temperature at point B (point where the temperature at the wick–fin interface is maximum) as a function of heat load.

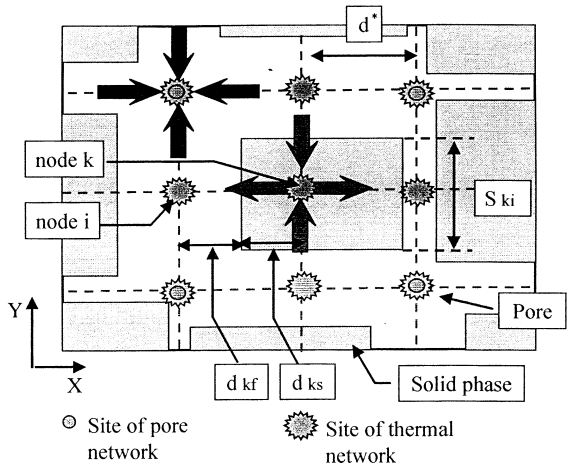

Fig. 9. Sketch of pore network model.

$$u_{ki}^{j} = -\frac{g_{ki}}{\mu_j}\frac{p_i - p_k}{d_{ki}} \tag{16}$$

In Equation (16), d_{ki} is the length of the throat, p_i the pressure at node i, p_k the pressure at the neighbor node connected to node i by throat k, g_{ki} is the flow conductivity of throat k which is classically expressed in terms of the hydraulic diameter d_h as

$$g_{ki} = \frac{d_h^2}{32}$$

with

$$d_h = \frac{4s_{ik}}{pe_{ik}}$$

where pe_{ik} is the throat perimeter and s_{ik} the throat section. In this approach, the pressure drop is assumed to be associated with throat only.

Equation (15) applies to nodes that are connected to neighbor nodes by bonds that do not contain a liquid–vapor interface (in this model, the meniscii are assumed to stabilize within bonds between two invasions). When a liquid–vapor interface is present in a bond, Equation (15) is modified for taking into account the mass flux due to the change of phase at the liquid–vapor interface. For instance, in the case of a vapor node having one bond containing a liquid–vapor interface, the mass balance is expressed as

$$\sum_k \rho_{ki}^{j} u_{ki}^{j} s_{ki} + \phi_m s_{4i} = 0 \quad k = 1, 3 \tag{17}$$

where ϕ_m is the mass flux associated with the change of phase in that bond. ϕ_m is deduced from the energy balance at the liquid–vapor interface as explained below.

Energy balance

Heat transfer by conduction in the solid, liquid and vapor phases was simulated as well as the heat transfer due to the change of phase. Radiative and convective heat transfer are negligible here compared to conductive and latent heat transfer and therefore have not been taken into account. To take into account the conductive heat transfer through the solid phase, a finer network than the pore network was considered, Fig. 9. This network is termed the thermal network. As can be seen from Fig. 9, the distance between two nodes of the thermal network is twice as small as the distance between two nodes of the pore space network. In addition to the nodes of the pore space network, complementary nodes are located in the

solid phase and in the middle of bonds. The energy balance for node i is expressed as follows:

$$\sum_k \lambda^*_{ki} \frac{T_i - T_k}{d^*} S_{ki} = 0, \quad k = 1,4 \tag{18}$$

where T_i is the temperature at node i, T_k the temperature at first neighbor node k. S_{ki} is the exchange surface between the considered nodes, Fig. 9, d^* is the distance between two nodes of thermal network. λ^*_{ki} is the thermal conductivity of segment k joining node i to neighbor node k which is first expressed according to a series arrangement model as (see Fig. 9 for the notations)

$$\lambda^*_{ki} = \frac{\lambda_s \lambda_f (d_{ks} + d_{kf})}{d_{ks}\lambda_f + d_{kf}\lambda_s} \tag{19}$$

where λ_f and λ_s are the thermal conductivities of solid and fluid (liquid or vapor) phases respectively. Equation (19) leads, however to underestimate the heat transfer by conduction since in our model the solid phase is not continuous but made of isolated grains. Hence, Equation (19) leads to exaggerate the influence of the conductive heat transfer in the fluid phase compared to the real three-dimensional system. In the present effort, this problem has been dealt with by using the following estimate instead of Equation (19),

$$\lambda^*_{ki} = \frac{\lambda_s \lambda_f^{ef} (d_{ks} + d_{kf})}{d_{ks}\lambda_f^{ef} + d_{kf}\lambda_s} \tag{20}$$

where λ_f^{ef} is the effective thermal conductivy of the porous medium saturated by liquid ($f = l$) or vapor ($f = v$), see Section 3.1. The essential point is that the apparent conductivities in each saturated zone, liquid or vapor, are about the same in the continuum and discrete approaches. As we shall see, Equation (20) leads to a satisfactory agreement with the continuum model predictions. Naturally, this part of the model could be modified and improved easily if necessary.

Boundary conditions

The boundary conditions are similar to the ones used for the continuum model, Equations (10)–(14), except for the thermal problem where flux conditions were imposed at the groove–wick interface, i.e.

$$\text{At } y = L_y \text{ and } L_f \leqslant x \leqslant L_x, \quad \lambda^* \frac{\partial T_i}{\partial y} = \phi/20, \quad i = l, v \tag{21}$$

The factor 1/20 in Equation (21) was deduced from a preliminary simulation of pure thermal conduction in the fin-groove region and is a direct consequence of the much lower thermal conductivity of the vapor compared to that of the metallic fin. Although this boundary condition is a little more satisfactory than the zero flux condition considered before, its influence on the results is weak. However, for the comparison between the two models, Section 4.2.1, Equations (10)–(14) were imposed.

The saturation temperature T_{sat} is imposed at each liquid–vapor interface.

Source term ϕ_m

The source term ϕ_m is determined on each liquid–vapor interface from the energy balance,

$$\frac{\phi_m}{L} = \lambda_v^{ef} \frac{T_v - T_{sat}}{d^*} - \lambda_l^{ef} \frac{T_{sat} - T_l}{d^*} \tag{22}$$

Numerical procedure

The numerical procedure can be summarized as follows. Initially the network is saturated by liquid except the first series of bonds underneath the fin which are saturated by vapor (in order to allow the vapor to escape from under the fin towards the groove). The temperature field is then determined by solving the system of equations defined by Equation (18). The source term at each liquid interface is deduced from Equation (22). This enables us to determine the pressure field by solving the system of Equations (15)–(17). Once the pressure field is known, the pressure difference ΔP across the liquid–vapor interfaces is determined and compared to the maximum pressure differences given by Laplace's law, i.e.

$$p_{ci} = \frac{2\sigma \cos\theta}{\delta_i}$$

where σ is the interfacial tension, θ the wetting angle (assumed equal to zero) and δ_i is the throat width. For some bonds, one found (except for sufficiently low heat loads) that $\Delta P > p_{ci}$, indicating that the stationary solution has not been reached. At this stage, various bond invasion criteria can be developed. The two we have used are the following: (1) only the bond associated with the maximum value of $\Delta P/p_{ci}$ is invaded, (2) all the bonds such that $\Delta P/p_{ci} > 1.1$ are invaded by vapor. Satisfactorily, both criteria lead to the same stationary solution [11]. Once the network phase distribution has been updated, the overall procedure is repeated until the stationary solution is obtained, i.e. until $\Delta P < p_{ci}$ on each liquid–vapor interface. Note that any isolated liquid cluster that forms is removed, i.e. all bonds and nodes belonging to such a cluster are declared to be occupied by vapor (in the present effort, mechanisms such as condensation, re-imbibition of pores by liquid, liquid film flows are neglected, therefore any isolated liquid cluster that forms must vaporize before the stationary solution is reached). The results presented in what follows were obtained for a 99×99 pore network, which corresponds to a 199×199 thermal network. It is worth noting that this number of pore ($\approx 10\,000$) is quite representative of real systems. Ammonia is the working fluid.

4.2. Results

4.2.1. Pore network simulation versus continuum model

In order to compare the two approaches, i.e. the pore network model and the continuum model, we assumed

that all bonds have the same width, $\delta = 10$ μm and we imposed the same boundary conditions as for the continuum model, Equations (10)–(14), with $\phi = 5000$ W m^{-2}. The physical properties of the various phases are equal to the ones used for the simulations with the continuum model presented in Section 3. Figure 10 shows the solutions of the two approaches. They are practically identical. The fact that both approaches lead to same results is confirmed in Fig. 11 that shows the evolution of the vapor zone size as a function of heat load. This indicates that the continuum model considered in the present paper and the similar one developed by Demidov and Yatsenko [4] are valid in the limit of an extremely narrow pore size distribution.

4.2.2. Pore network simulations

In this section, the influence of some disorder in the pore size distribution is investigated. The bond widths

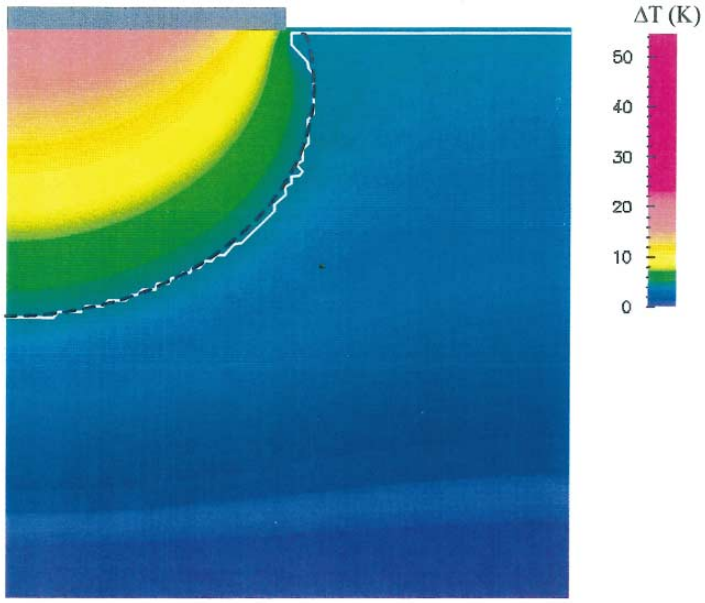

Fig. 10. Pore network simulation versus continuum model solution. Liquid–vapor front position: black dot line—continuum model; white solid line—network model. $\phi = 5000$ W m^{-2}; $\Delta T = T - T_0$.

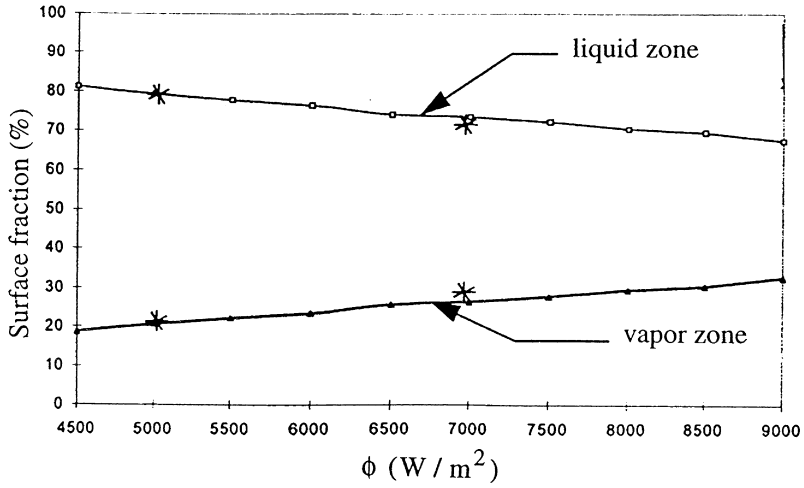

Fig. 11. Vapor zone and liquid zone surface fraction as a function of heat load: * network model, —— continuum model.

are uniformly distributed between δ_{min} and δ_{max} with a bond average width kept equal to 10 μm. The ratio between the smallest width and the largest one is noted R, $R = \delta_{max}/\delta_{min}$. Increasing R corresponds to an increase in the pore structure disorder. The solid thermal conductivity is $\lambda_s = 10$ W m^{-1} K^{-1}. Thus, in this series of simulations, a thermal conductivity corresponding to a highly conductive solid phase was used. The permeability slightly varies as a function of R in the range 3.2–3.4×10^{-13} m^2. The porosity is $\varepsilon = 0.435$. The boundary conditions were specified as explained before with $T_0 = 10$°C, $P_0 = P_1 - 40$ Pa, where P_1 is the pressure of the vapor in the groove.

4.2.2.1. *Vapor zone extension as a function of heat load.* The simulations presented in this section were performed for $R = 2$ and heat loads in the range 5000–200 000 W m^{-2}. For heat loads lower than about 10 000 W m^{-2}, the wick is not invaded by vapor, i.e. for each liquid–vapor interface located in the first series of bond underneath the fin the pressure differences across the interface is lower than the capillary threshold given by Laplace's law. This is illustrated in Fig. 12. As can be seen from Fig. 12, there exists a vapor pressure gradient under the fin. This gradient is associated with the vapor flow towards the groove along the fin. When the heat load becomes sufficiently high, the pressure difference across some liquid–vapor interfaces becomes greater than the capillary pressure threshold of the associated bonds. Therefore, the vapor invades the wick until a stationary solution is obtained, i.e. until the interface pressure difference is lower than the capillary pressure threshold for each elementary interface forming the front. This is illustrated in Figs. 13 and 14. As can be seen from Fig. 14, the front is not smooth as before but highly irregular. Naturally, as the heat load is further increased, the vapor zone

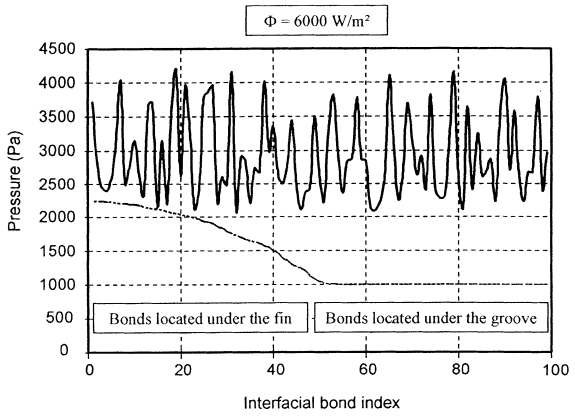

Fig. 12. Distribution of local capillary pressures (smooth line) and capillary pressure thresholds (irregular line) along the liquid–vapor interface for an almost liquid saturated wick.

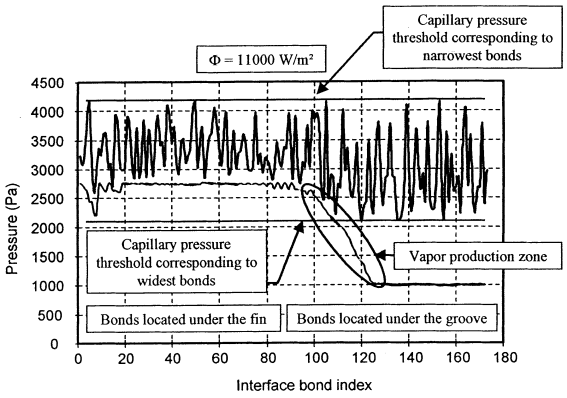

Fig. 13. Distribution of local capillary pressures (smooth line) and capillary pressure thresholds (irregular line) along the liquid–vapor interface for the stationary solution corresponding to $\phi = 11\,000$ W m^{-2}.

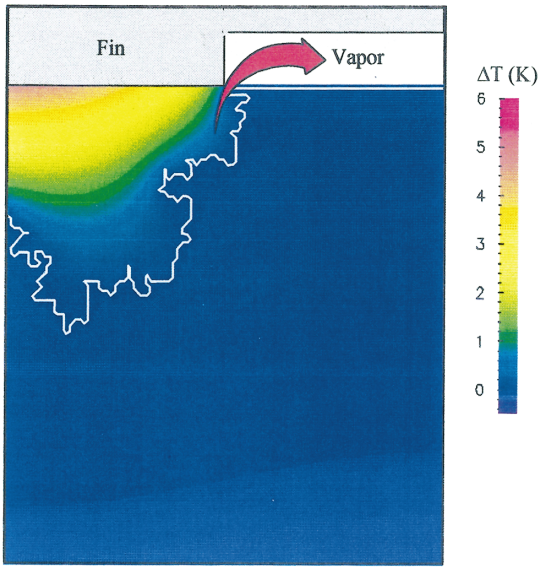

Fig. 14. Temperature field and liquid–vapor front for $\phi = 15\,000$ W m^{-2} and $R = 2$; $\Delta T = T - T_0$.

increases as shown in Fig. 15. It is interesting to observe that the vapor zone extension is not a simple function of heat load. As can be seen from Fig. 15, the location of the front is practically the same for heat loads varying from 15 000 to 35 000 W m^{-2}. The pinning of the front can be expected when most of the liquid–vapor interfaces become located in relatively narrow bonds. Together with the rough shape of the front, the front pinning is a consequence of the local capillary pressure thresholds distribution. When the heat load is about equal to 200 000 W m^{-2}, the vapor breakthrough is obtained. Naturally, the

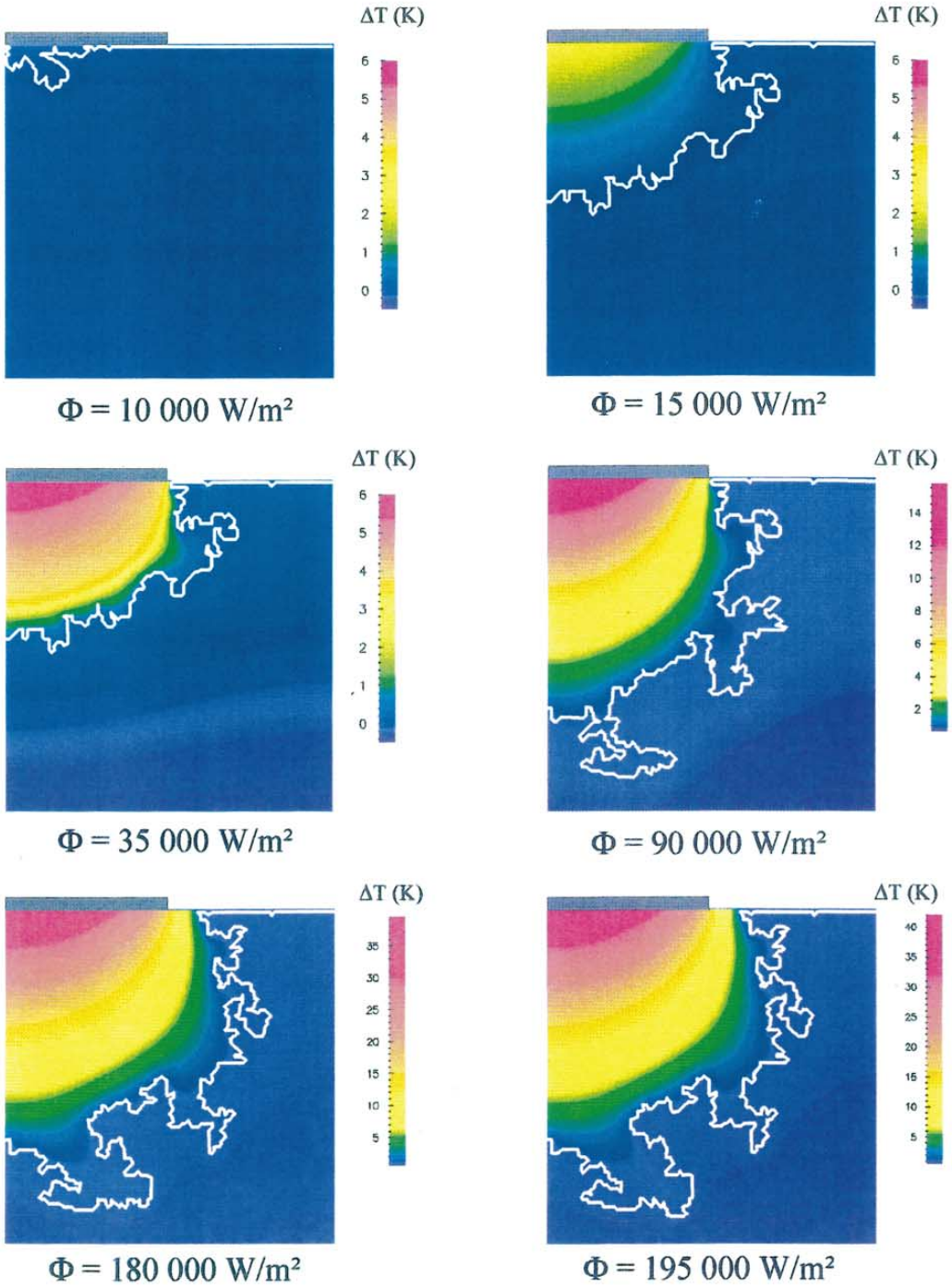

Fig. 15. Temperature fields and liquid–vapor fronts as a function of ϕ ($R = 2$); $\Delta T = T - T_0$.

vapor breakthrough should be avoided when operating a CPL (the vapor breakthrough may lead to sudden deprime of the loop). The growth of the vapor zone is associated with the increase of the fin superheat as shown in Fig. 16. As can be seen from Fig. 16, the fin superheat is practically zero as long as the wick is saturated. The

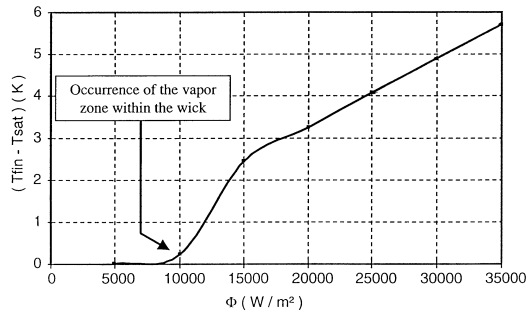

Fig. 16. Fin superheat as a function of heat load.

superheat increases as the vapor zone increases. The change in the slope in Fig. 16 for $\phi = 15\,000$ W m^{-2} can be explained by the fact that significant invasions of bonds in the fin corner region occurs only for $\phi \geqslant 15\,000$ W m^{-2}.

4.2.2.2. *Influence of pore size distribution*. The influence of the pore size distribution was further explored by varying R between 1 and 5 for $\phi = 35\,000$ W m^{-2}. The results reported in Fig. 17 indicate that the bond width heterogeneity may favor the invasion of the vapor. In particular, it is interesting to observe that the vapor breakthrough is nearly obtained for $R = 5$ while the vapor breakthrough can be expected to occur with significantly greater heat load for $R = 1$. Note that the capillary capacity of the wick, i.e. the average pore size, is about the same for $R = 1$ and $R = 5$.

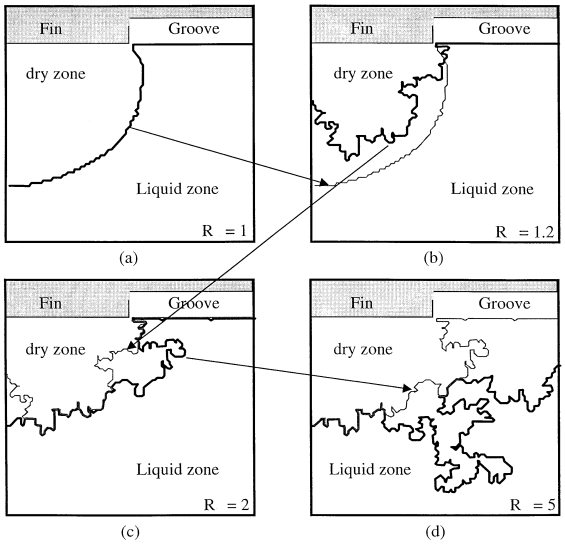

Fig. 17. Influence of R (spreading factor of pore size distribution) on the front shape and position.

4.2.2.3. *Influence of wick thermal conductivity*. The influence of the wick thermal conductivity was briefly explored. For otherwise identical conditions, simulations were performed for $\lambda_s = 10$ W m^{-1} K^{-1} and $\lambda_s = 0.5$ W m^{-1} K^{-1}. The results are presented in Figs. 18 and 19. An interesting result, illustrated in Fig. 19, is that the front position is nearly independent of λ_s here. This is not surprising since, with the boundary conditions that are imposed in the simulations, the heat flux are necessarily identical. Naturally, this implies significant differences in the temperature distributions as shown in Figs. 18 and 19. As expected, the fin superheat is much greater with a low thermal conductivity wick, Fig. 19.

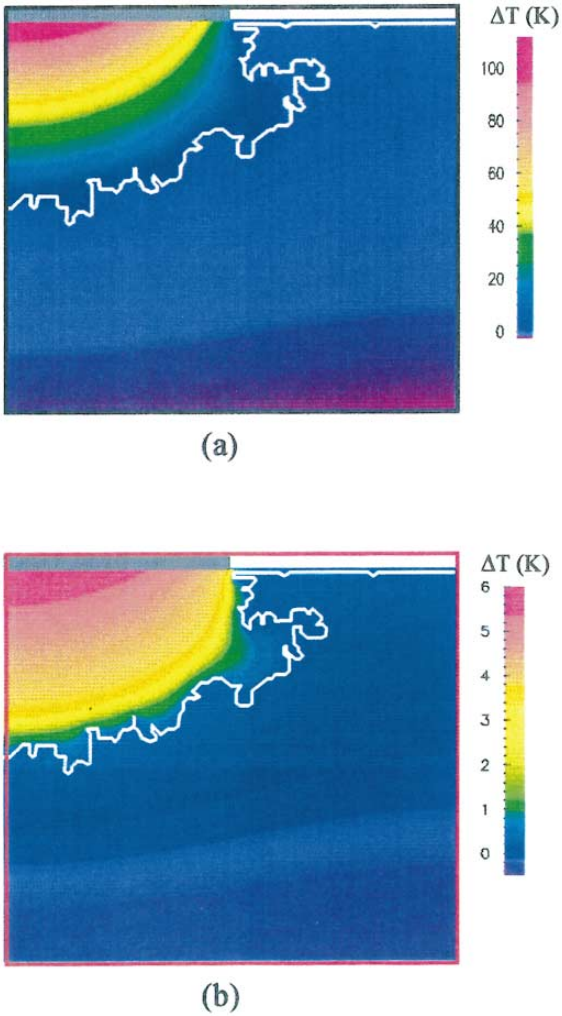

Fig. 18. Influence of the wick thermal conductivity on the front shape and temperature distribution for $\phi = 35\,000$ W m^{-2}: (a) $\lambda_s = 0.5$ W m^{-1} K^{-1}; (b) $\lambda_s = 10$ W m^{-1} K^{-1}; $\Delta T = T - T_0$.

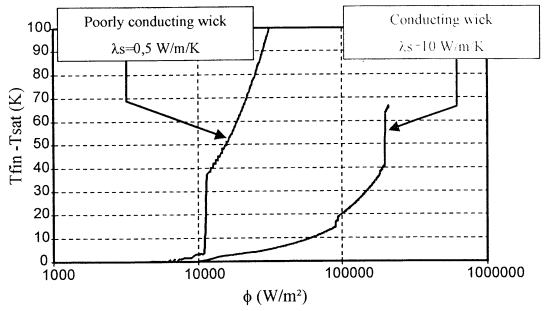

Fig. 19. Influence of wick thermal conductivity of the fin superheat.

5. Discussions

In this section, we first discuss briefly why the shape of the liquid–vapor interface is characteristic of capillary fingering [8], when there is some disorder in the pore structure, i.e. when $R > 1$. Second, we suggest an improved design of the wick directly inferred from the results presented in the present paper.

In the pore network or discrete approach, the convergence towards the stationary solution can be viewed as an immiscible displacement in which vapor, which is here the non-wetting fluid, displaces liquid ammonia. Therefore, one may expect similarities with drainage patterns (displacement of a wetting fluid by a non wetting fluid). These depend on the viscosity ratio and the capillary number,

$$Ca = \frac{u\mu}{\sigma}$$

where u and μ are the velocity and the viscosity of the displacing (non-wetting) fluid. Ca is in fact the ratio of the pressure drop associated with viscous effects to the capillary pressure jump. As capillarity is here the driving force, it is clear that operating stationary conditions are necessarily associated with small capillary numbers, i.e. capillary dominated process. At very low Ca, drainage patterns obey the invasion percolation [17]. Invasion percolation applies, however, in the quasi-static limit only. Here, it is clear that viscous forces do affect the selection of the invaded bonds, as illustrated for example in Fig. 12. If one notes that the displacing fluid is less viscous than the displaced fluid, corresponding drainage patterns are in the cross-over region between invasion percolation and DLA (Diffusion Limited-Aggregation) patterns [8]. The analogy with drainage does not strictly hold here however. An important difference is that, in the phase change process under study, the displaced fluid flows not in the same direction as the front displacement but in the opposite direction, i.e. towards the front. Contrary to conventional drainage, this leads to pressure gradients that tend to stabilize the front [7, 18]. In other terms, since capillarity controls the process but viscous effects are not negligible, it is finally not surprising to obtain stabilized fractal fronts similar to the ones observed when gravity or viscous effects act as a stabilizing force in an invasion percolation process [6, 7, 13]. For instance, it is known from gradient invasion percolation [13], that the front width increases as the capillary number decreases. This is consistent with the influence of the pore size distribution described in Section 4.2.2. Although the standard definition of the capillary number does not take into account the influence of R, a little thought indicates that increasing R amounts here to diminishing Ca.

From a practical standpoint, the results suggest an improved design along the lines discussed hereafter. As far as the wick thermal conductivity is concerned, the results show that the use of a high conductivity limits the superheat of the fin. On the other hand, using a high thermal conductivity may favor the liquid boiling at the entrance of the wick for the low heat loads. Regarding the fluid transport, it seems interesting to use a relatively high permeability in the vapor zone in order to make the vapor flow easier. High permeabilities are generally associated with low capillary potentials, which is not particularly interesting since capillarity is the driving force. This suggests to develop a layered wick made of porous layers having different properties. In [19], a two layers system was considered. The first layer, in the vicinity of the fin, has relatively high thermal conductivity and permeability while the second layer is characterised by smaller pores and a low thermal conductivity (the small pores stop the development of capillary fingering). The pore network simulations reported in [19] as well as the results reported in [9] for a more refined three layers system show that this type of design is attractive and would certainly deserve a more extensive study.

6. Conclusions

Two numerical tools were developed and applied to the study of coupled heat and mass transfers in the porous structure. An excellent agreement was found between the predictions of the two models when the porous structure is characterized by a single pore size. When the pore size varies, capillary effects lead to fractal type fronts that cannot be predicted by the continuum model. The pore network simulations indicate that the capillary effects associated with some distribution in the pore size can restrict the performance of the evaporator compared to the single pore size case. Although the developed network model can be regarded as preliminary and is certainly questionable on some aspects, the results presented in this paper show that pore-network models can be useful tools for studying complex phase change phenomena in porous media. As far as the particular problem considered in this paper is concerned, it would be interesting

to develop three dimensional network models since it is known from the immiscible displacement studies that three dimensional phase distributions can be expected to be different from the two dimensional ones. In particular, it is expected that three-dimensional simulations would lead to significantly lower superheat of the fin than the somewhat large superheat computed with two-dimensional models (vapor and liquid phases are expected to form two tangled 'infinite' clusters in 3D). Conducting experiments at the pore network level would also be interesting, either in order to confirm the findings of the present paper or possibly to identify mechanisms not included in the present model.

Acknowledgements

Financial support from Matra Marcony Space (MMS) and CNES (French national center for space studies) are gratefully acknowledged. C.F. was supported by a BDI grant from CNRS and CNES. Y.L.B. was supported by a grant from the French Ministère de l'Education.

References

[1] D.R. Chalmers, J.J. Pustay, C.B. Moy, E.J. Kroliczeck, Application of capillary pumped loop heat transport systems to large spacecraft, Proceedings of the AIAA/ASME Fourth Joint Thermophysics and Heat Transfer Conference, Boston, MA, 1986.

[2] Y. Cao, A. Faghri, Conjugate analysis of a flat-plate type evaporator for capillary pumped loops with three-dimensional vapor flow in groove, Int. J. Heat and Mass Transfer 37 (3) (1994) 401–409.

[3] Y. Cao, A. Faghri, Analytical solutions of flow and heat transfer in a porous structure with partial heating and evaporation on the upper surface, Int. J. Heat and Mass Transfer 37 (10) (1994) 1525–1533.

[4] A.S. Demidov, E.S. Yatsenko, Investigation of heat and mass transfer in the evaporation zone of a heat pipe operating by the inverted meniscus principle, Int. J. Heat and Mass Transfer 37 (14) (1994) 2155–2163.

[5] M. Prat, Percolation model of drying under isothermal conditions in porous media, Int. J. Multiphase Flow 19 (4) (1993) 691–704.

[6] M. Prat, Isothermal drying of non-hygroscopic capillary-porous materials as an invasion percolation process, Int. J. Multiphase Flow 21 (5) (1995) 875–892.

[7] J.B. Laurindo, M. Prat, Numerical and experimental network study of evaporation in capillary porous media: phase distributions, Chem. Eng. Sci. 51 (23) (1996) 5171–5185.

[8] R. Lenormand, E. Touboul, C. Zarcone, Numerical models and experiments on immiscible displacements in porous media, J. Fluid Mech. 189 (1988) 165–187.

[9] C. Figus, N. Dunbar, S. Bories, W. Supper, Experimental evaluation of a novel microscopic model of a capillary pumped evaporator, Proceedings of the Sixth European Symposium on Space Environmental Control Systems, ESA Publication Division, pp. 377–383.

[10] G. Dhatt, G. Touzot, Une présentation de la méthode des éléments finis, S.A. Maloine (Ed.), Les Presses de l'Université Laval, Quebec, 1981.

[11] C. Figus, Transfert de chaleur et de masse avec changement de phase en milieux poreau: application à un évaporateur capillaire, INPT thesis, Toulouse, France, 1996.

[12] C. Figus, S. Bories, M. Prat, Investigation and analysis of a porous evaporator for a capillary pump loop, in: R.M. Eslami, A.A. Becker, R. Ohayon, A. Faghri, A. Chrysochoos (Eds.), Proceedings of the 1996 Engineering Systems Design and Analysis Conference, vol. 8, ASME-ESDA, 1996, pp. 99–106.

[13] M. Sahimi, Flow and Transport in Porous Media and Fractured Rock, VCH, 1995.

[14] X. Li, Y.C. Yortsos, Visualization and simulation of bubble growth in pore networks, AIChE J. 41 (1995) 214–222.

[15] Y. Le Bray, Contributions à l'étude du changement de phase liquide-vapeur en milieu poreux. Simulations numériques sur réseaux de pores, INPT thesis, Toulouse, France, 1997.

[16] C. Satik, Y.C. Yortsos, A pore-network study of bubble growth in porous media driven by heat transfer, ASME J. Heat Transfer 118 (1996) 455–462.

[17] D. Wilkinson, J.F. Willemsen, Invasion percolation: a new form of percolation theory, J. Phys. A: Math. Gen. 16 (1983) 3365–3376.

[18] T.M. Shaw, Drying as an immiscible displacement process with fluid counterflow, Phys. Rev. Lett. 59 (15) (1987) 1671–1674.

[19] C. Figus, Y. Le Bray, S. Bories, M. Prat, Heat transfer in porous media considering phase change, capillarity and gravity: Application to capillary evaporators. Proceedings of the 11th International Heat Transfer Conference, Kyongju, 1998, vol. 4, pp. 393–398.